Three-Dimensional Integrated Optics Using Polymers

Sean M. Garner, Sang-Shin Lee, Vadim Chuyanov, Antao Chen,
Araz Yacoubian, William H. Steier, and Larry R. Dalton

***Abstract*— Some of the key components are demonstrated to make three-dimensional (3-D) optical integrated circuits possible using polymers. Fabrication techniques of shadow reactive ion etching, shadow photolithography, and gray-level photolithography to produce complex 3-D integrated optic structures are demonstrated. Vertical waveguide bends exhibit excess losses of $<$0.3 dB, and vertical power splitters possess predictable output splitting ratios between multiple core levels with excess losses of $<$0.5 dB. Vertical polarization splitters exhibit power extinction ratios of 15 dB between the output core layers. A 1 $\times$ 4 vertical–horizontal power splitter is also demonstrated. Additionally, these techniques are used to integrate different polymer materials into the same optical circuit while easily solving the mode mismatch problem. To show the technique, a polymer electrooptic modulator is vertically integrated with a low-loss waveguide.**

***Index Terms*— Birefringence, electrooptic devices, integrated optics, optical interconnections, optical polymers, optical waveguides, waveguide bends, waveguide components.**

I. Introduction

CONVENTIONAL two-dimensional (2-D) guided wave integrated optics provides a reliable and structurally stable method for interconnecting optical devices in photonic circuits and for the optical interconnection of high-density integrated electronics. However, in two dimensions, the complexity of the photonic circuits is limited by the size of the substrate and by the difficulty of connecting a large number of input and output fibers or electrical connections. For the optical interconnection of dense electronic circuits, the limitation of two dimensions restricts the interconnection density to relatively low numbers and makes free space optical interconnections look more promising. This is because the routing of a large number of waveguides in two dimensions inevitably involves a large number of waveguide crossings with their accompanying excess loss and crosstalk.

The possibility of adding the third dimension to integrated optics would greatly increase the integration density and would overcome some of the input–output problems while preserving the reliability and structural stability of guided wave optics. The concept of three-dimensional (3-D) integrated optics is shown in Fig. 1. It consists of vertically stacked layers of horizontal 2-D integrated optics with appropriately placed vertical waveguide interconnects between the layers. The third dimension significantly increases the possible density of both optical and electrical inputs and outputs. The stacked layers allow routing of waveguides around obstacles and eliminate waveguide cross-over losses. The concept of 3-D integrated optics can make guided wave interconnects with the same density and efficiency as free space holograms but with greatly increased stability [1].

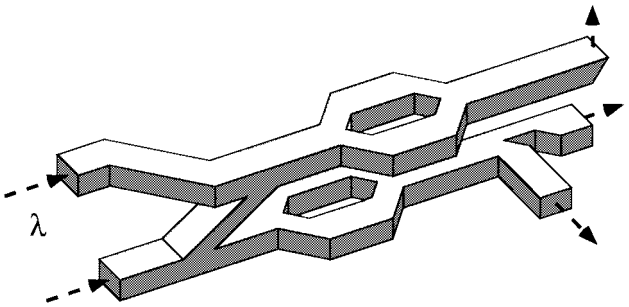

Fig. 1. General design of 3-D integrated optics. (Only the waveguide core is shown for clarity.)

Optical polymers have some significant advantages over other materials such as semiconductors or silica as a material for 3-D optical integration. The vertical features can be etched by using shadow mask etching or a photoresist as the etch mask. Photoresist is an appropriate etch mask since the etch rate of most polymers is similar to that of photoresist. In addition optical polymers can have excellent adhesion to a number of surfaces, and, by varying the doping level or by combining multiple polymer systems, precise control of the index of refraction is possible. Polymers have also been demonstrated with very low optical loss and good environmental stability [2].

In this paper, we present some of the designs and experimental results on realizing the key components which can make 3-D integrated optics in polymers a practical reality. These single-mode structures include vertical waveguide bends, vertical waveguide power splitters including a 1 $\times$ 4 vertical–horizontal structure, and vertical waveguide polarization splitters. We also show how these concepts can lead to the vertical integration of active and passive polymer materials in order to incorporate electrooptic and, possibly, light-amplifying polymers into an integrated circuit.

II. Fabrication of Three-Dimensional Structures

There have been limited reports of fabrication techniques for vertical optical structures in polymers. The techniques typically used are photobleaching and embossing. Controlled

Manuscript received October 30, 1998; revised May 11, 1999. This work was supported by the Air Force Office of Scientific Research and the Office of Naval Research.

S. M. Garner, S. Lee, V. Chuyanov, A. Chen, A. Yacoubian, and W. H. Steier are with the Department of Electrical Engineering-Electrophysics, University of Southern California, Los Angeles, CA 90089-0483 USA.

L. R. Dalton is with the Department of Chemistry, University of Southern California, Los Angeles, CA 90089-1062 USA.

Publisher Item Identifier S 0018-9197(99)05947-3.

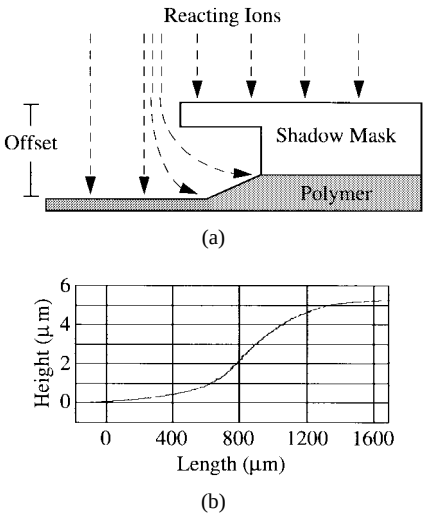

Fig. 2. Shadow RIE technique for slope etching. (a) Schematic of etching method. (b) Profile of the etched slope.

photobleaching of polymers which contain chromophores can create a depth-dependent index variation [3] and has been used to fabricate tapered waveguides. Replication methods of embossing and molding allow mass production of integrated optical components and have been used for low-cost microstructures [4]. These methods, however, are not suitable for constructing vertical waveguide interconnects among multiple layers. To fabricate 3-D integrated optical structures, we employed reactive ion etching (RIE) in O_2 and CF_4 to etch low-angle slopes in the polymer layers, either directly by shadow masks or through intermediate patterned photoresist layers.

A. Shadow Mask Reactive Ion Etching (RIE)

This approach of directly etching a slope in a polymer layer involves placing a shadow mask on the polymer surface before placing the sample into the reacting chamber. Fig. 2 illustrates both the shadow RIE technique and a typical slope as measured with a Sloan Dektak IIA profilometer. The presence of the mask overhang produces a variable etch rate across the surface of the film. The masks consisted of standard microscope slides supported at the edges approximately 2 mm above the polymer surface.

By controlling the gas pressure, RF power, etching time, and physical dimensions (overhang offset and length) of the mask, predictable S-curved vertical slopes can be etched by using calibration curves for each parameter [5]. A good empirical curve fit to the stretched-S shaped slope produced by the RIE etch is provided by [5, eq. (1)]. The horizontal and vertical function coordinates are $\mathbf{x}$ and $\mathbf{y}$, while $\mathbf{h}$ and $\mathbf{l}$ are the overall slope height and length, respectively:

$$y = \frac{h}{1 + \exp(8 \times /1)}. \tag{1}$$

The parameters $\mathbf{h}$ and $\mathbf{l}$ have been experimentally measured for a variety of etch conditions in [5]. For example, to produce smoothly etched surfaces in the polymer films, we used the following conditions with a typical parallel-plate plasma etcher: both O_2 and CF_4 gases [6] at flow rates of 25 and 10 sccm, a chamber pressure of 400 mtorr, and an RF power density of 0.15 W/cm^2. A 60-min etch typically yields $\mathbf{h}$ and $\mathbf{l}$ values of 5.5 and 1.4 μm, respectively. In general, more directional etches (higher pressure, etc.) and larger spacing between the mask and the surface to be etched yield larger slope angles and shorter slope lengths.

With this method, we have produced slope angles ranging from 0.1° to 3° with etch depths of up to 15 μm. This etch depth was limited only by the thickness of the polymer films. Slope lengths typically ranged from 0.1 to 2 mm. This wide variety of taper dimensions enables fast prototyping of new 3-D device designs, and it avoids time-consuming photolithography steps.

B. Partial Exposure Photolithography

Another method for producing vertical structures in polymers involves first creating 3-D features in a photoresist overlayer and then transferring them with standard RIE techniques to the underlying polymer film. To produce the vertical features, the first step relies on the partial exposure of the photoresist either by shadow lithography or gray-level lithography and subsequent development of the photoresist. The vertical feature in the photoresist can be transferred to the underlying optical polymer layer by RIE because the optical polymers and photoresist have similar etch rates, typically ranging from 0.03 to 0.12 μm/min. In some cases, there is a slight difference in etch rates which enable expanding or contracting the vertical features while transferring them to the optical polymers. In this technique, the photoresist layer must be as thick as or thicker than the vertical height of the slope being transferred. We used photoresist AZ 5214E (Hoescht Celanese) for film thicknesses of up to 3.5 μm and AZ P4620 for films up to 6 μm. For deeper topographies, we either spun multiple photoresist layers or made multiple processing cycles. To fully develop these thick photoresist layers requires some agitation while in the developer solution.

The vertical features in the photoresist can be periodically measured and precisely controlled before permanently etching the optical polymer. Since the slope characteristics depend on both the exposure and development times with either AZ 400K or AZ 421K developers, the feature dimensions can be fine tuned after Dektak measurements. If the optical polymer is crosslinked or otherwise hardened to be resistant to solvents, misaligned or poor-quality photoresist patterns can be easily removed and the process repeated. Finally, the use of a standard mask aligner (Karl Suss-MJB3) allows precision in both the alignment and exposure of the photoresist patterns. Use of either the shadow or gray-level photolithography mask, described below, produces high-quality vertical photoresist structures.

1) Shadow Photolithography: Shadow photolithography consists of using a standard straight-edge mask pattern, vertically offset from the sample, to produce a variable exposure of the underlying photoresist. Fig. 3(a) illustrates this technique. The variable exposure is due to the diffraction and reflections of the ultraviolet (UV) light. Fig. 3(b) shows

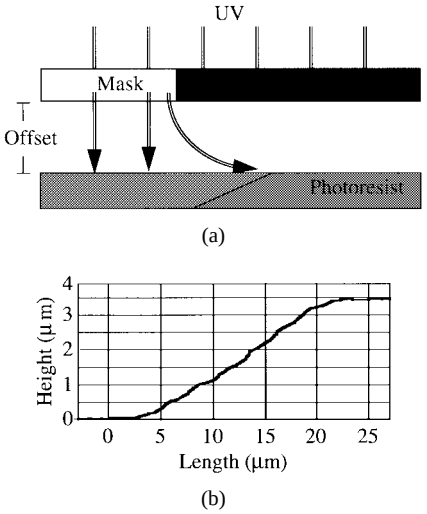

Fig. 3. Shadow photolithography technique for slope etching. (a) Schematic of etching method. (b) Profile of etched slope.

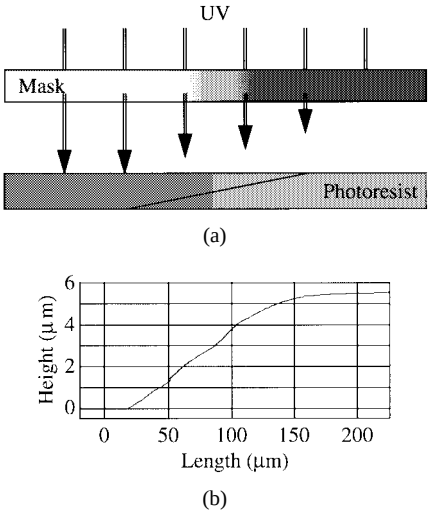

Fig. 5. Gray-level photolithography technique for slope etching. (a) Schematic of etching method. (b) Profile of etched slope.

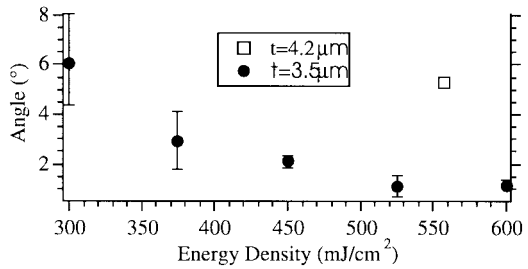

Fig. 4. Control of slope angles using shadow photolithography. Measured slope angle as a function of mask aligner exposing energy density. Data shown for two photoresist thicknesses, t.

a typical slope produced. It has a height of 4 μm and a length of 20 μm. Because of the collimated light from the mask aligner source, the resulting slopes possess large angles ranging from 1° to 13° in photoresist thicknesses of up to 5 μm. For this technique, we typically used the AZ 5214E photoresist because of the shorter exposure times it required.

The resulting vertical slope depends on the exposing energy density, photoresist thickness, and mask vertical offset. Varying any of these parameters allows control of the slope angle, and this exposure process must be calibrated. Fig. 4 shows the dependence of slope angle on exposing energy density for photoresist thicknesses of 3.5 and 4.2 μm. A constant mask vertical offset of 600 μm was used. With an exposing power density of 5 mW/cm^2, we easily produced a wide range of repeatable angles by varying the exposing time from 1 to 2 min. Because shadow photolithography produces a variety of angles with a single mask, it enables fast prototyping of new device designs.

2) Gray-Level Photolithography: Gray-level photolithography consists of using a variable transmission mask to partially expose the photoresist. Fig. 5(a) illustrates this method. The position-dependent transmission of the mask produces the variable UV exposure of the photoresist. This technique allows the transfer of very complex patterns to the entire photoresist film with a single exposure. Fig. 5(b) shows a typical slope produced. It has a height of 5.5 μm and a taper length of 100 μm. The lower bend angle only appears sharp because of the different scales of the two axes. Using this method, we produced slope angles ranging from 0.1° to 3° in film thicknesses of up to 15 μm. Additionally, the use of either AZ 5214 or AZ P4620 produced high-quality slopes.

We fabricated the transmission mask by transferring a computer-generated gray-scale image onto a holographic film plate (AGFA 8E56 HD NAH) [7]. The masks provided feature resolution of about 10–15 μm and produced smooth photoresist slopes with total lengths of 0.1–2 mm. The fabrication of these long slope lengths did not require higher resolution gray-level masks. Alternative mask sources include: commercial vendors,[1] fabricating from a spatially filtered half-tone image [8], and direct electron beam writing on a dosage sensitive substrate [9].

The advantage of gray-level photolithography lies in the ability to create arbitrary and complex surface topographies in photoresist films. Fabrication of 32 level diffractive optical elements with one exposure have been reported [7]. A single complex mask could be used to fabricate many vertical features in one processing step in the manufacturing of complex 3-D optical circuits.

C. Fabrication Summary

In summary, three specific methods exist for creating vertical structures in optical polymers. These include shadow RIE, shadow photolithography, and gray-level photolithography. Shadow RIE generally creates small slope angles of $<3°$. It does not require any extensive processing steps, so it is ideal for prototyping new device designs. Shadow photolithography, on the other hand, generally creates larger slope angles of 1°–13°. The use of the mask aligner, however, allows precise alignment and timing of the exposure that is not possible with the RIE technique. Finally, gray-level photolithography allows the most freedom in vertical structure fabrication. The mask aligner and transmission of the gray-level mask enable precise control of the developed photoresist features. Although they

[1] See, for example, Sine Patterns LLC, East Rochester, NY.

offer varying degrees of processing control, each of the three fabrication techniques enable vertical structures for practical 3-D integrated optics. The rest of this paper discusses a few representative and key optical elements for the 3-D integration of optical waveguide devices.

III. Applications of 3-D Structures

The ability to fabricate vertical features, particularly gentle vertical slopes, makes possible the key elements to realize complex 3-D integrated optics. The key single-mode elements that we have demonstrated are vertical waveguide bends, power splitters, and polarization splitters to provide routing of the optical power between multiple vertical levels. We have also demonstrated the integration of polymer electrooptic switches and modulators with passive polymer integrated optics using the 3-D approach.

In all of these structures, additional layers must be spun on top of the vertically patterned slopes to make the upper waveguiding layers. For slope angles of a few degrees, spin casting additional films of <5-μm thicknesses preserves the original surface contour. Thicker films or steeper angles cause a planarization effect of the surface features which must be taken into account in the device design.

A. Vertical Waveguide Bends

Similar to the 2-D case, vertical waveguide bends are a necessary component for practical 3-D integrated optics for the low-loss transfer of power between the layers. Vertical directional couplers [10] have previously been used to transfer power between different waveguide cores. These devices, however, are very sensitive to wavelength and fabrication tolerances of the waveguide dimensions. The design and fabrication of the vertical waveguide bends described below provides the basis for more complicated structures such as vertical power and polarization splitters.

1) Fabrication: The fabrication of vertical waveguide bends involved first spin casting an 11-μm UV15LV (Master Bond) lower cladding layer onto a Si substrate. This thickness required two subsequent spinning/curing cycles. To achieve high-quality films, the UV15LV must pass through a 0.2-μm filter before spin casting. Next, a 1.6° slope with a height of 3.0 μm was etched across half of the sample with the methods described in Section II. The final steps included spin casting a 2.0-μm NOA-73 (Norland) guiding layer, etching a waveguide with a 0.3-μm ridge, and then spin casting an additional 4.6-μm UV15LV upper cladding layer. All films were UV cured. This creates standard straight waveguides and vertical waveguide bends on the same sample with waveguide widths varying from 1 to 6 μm. For the core and cladding materials, the refractive indices at $\lambda = 1.31$ μm are 1.542 and 1.510, respectively. Cutting the samples with a dicing saw to a length of 1 cm provided high-quality endfaces for fiber coupling. Fig. 6 illustrates the waveguide bend test sample.

2) Experimental Results: To evaluate the vertical waveguide bends, polarized light ($\lambda = 1.31$ μm) from a standard single-mode optical fiber was launched into the waveguide. The output was collected with a 60× microscope objective lens and focused onto a calibrated detector. Comparing the output power of the vertical waveguide bends with the adjacent straight waveguides demonstrated an excess loss value as low as 0.2 dB. Excess loss is defined as the ratio of the power out of a vertical bend waveguide to that of an adjacent straight waveguide using the same light input and output conditions as much as possible. The accuracy of this measurement depends on the repeatability of the input and output conditions and is estimated to be 0.1 dB.

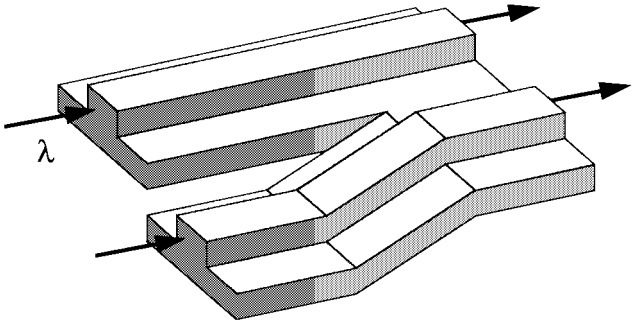

Fig. 6. Vertical waveguide bend test sample. Three-dimensional waveguide bends fabricated adjacent to straight waveguides. (Only the waveguide core is shown for clarity.)

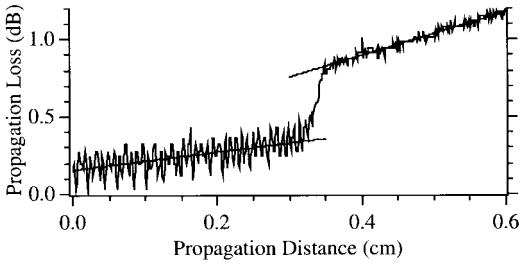

Fig. 7. Propagation loss as a function of length for a slab vertical waveguide bend at $\lambda = 1.31$ μm. (Discontinuity corresponds to vertical slope position.)

We were able to confirm this low excess loss for similarly fabricated slab waveguide bends by using the liquid outcoupling measurement technique developed by Teng [11]. In this method, light is coupled into a slab mode and is outcoupled at the surface of a high index liquid as the sample is immersed in the liquid. The slope of a plot of the output power as a function of the depth of immersion gives the propagation loss, which is independent of the input coupling efficiency. Fig. 7 shows this plot for a slab waveguide with a vertical bend. The 0.5-dB discontinuity in the propagation loss corresponds to the position of the vertical bend. The accuracy of this measurement is limited by the linear curve fitting of the power fluctuations. Typically, this error is estimated to be 0.3 dB.

Fig. 8 shows the TE and TM polarization insertion losses for various waveguide widths. These insertion losses include fiber coupling at the input, material loss, and propagation loss in the waveguide. We observed losses independent of both the polarization and propagation direction. All waveguides were designed to be single mode at 1.31 μm. Finally, viewing the waveguide patterns with a scanning electron microscope showed high-quality photolithography definition throughout the structure even though the levels differ substantially in

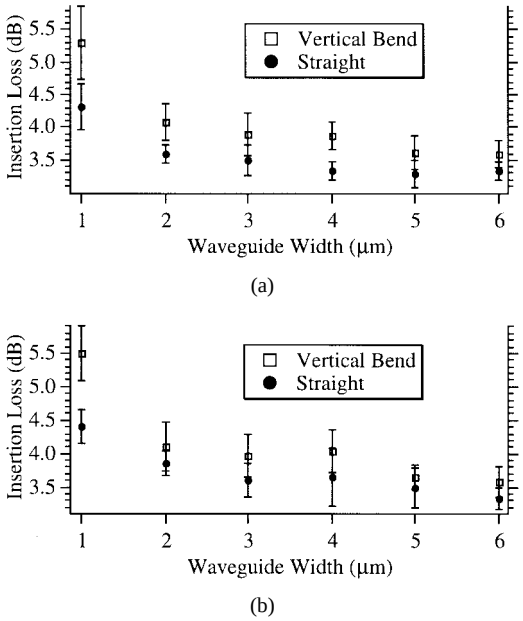

Fig. 8. Insertion loss for vertical waveguide bends and straight waveguides at $\lambda = 1.31$ μm (all waveguides are 1 cm in length). (a) TE polarization. (b) TM polarization.

vertical height. Two-dimensional beam propagation simulations (RSoft) predicted radiation losses of only 0.05 dB when representing the bend as a cosine S-curve [12], [13]. We therefore suspect that the measured excess losses are dominated by scattering loss which could possibly be reduced by improvements in the etching procedure.

The vertical bends are characterized by the relatively large index difference between the core and the cladding, typically $>$0.03. Because of the large vertical index difference, the vertical bends can have much smaller turning radii than is characteristic of horizontal bends when the horizontal patterning is done with ridge waveguides. For example, to move the mode up 5 μm in a vertical bend required only a 110-μm transition length. The smaller horizontal effective index difference, however, requires a total bend length of $>$1600 μm to horizontally displace the optical mode the same relative distance with an equivalent radiation loss.

B. Vertical Power Splitters

Analogous to asymmetric Y-branches, vertical power splitters divide the optical power among multiple vertical layers. Their design consists of optimizing the coupling of the input optical mode to the modes of the output waveguides, maintaining the optical isolation of the outputs, and reducing the radiation loss within the branching region.

To divide the optical power arbitrarily among the output waveguides, the splitter must act as a nonadiabatic device. Nonadiabatic structures are characterized by relatively large branching angles. The result is that the ratio of the output optical powers depends on the difference in propagation constants of the two output waveguides and the incorporated branch angle [14]. In contrast, adiabatic devices have relatively small branching angles and the input power is coupled completely

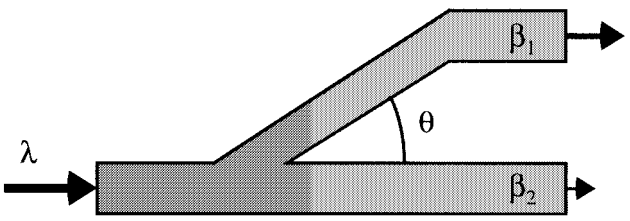

Fig. 9. Asymmetric Y-branch design for vertical power splitter. The output power splitting ratio depends on the propagation constants β for the branch waveguides and the branching angle θ.

to the output branch whose propagation constant most nearly matches that of the input waveguide [14].

The vertical power splitters we have fabricated are nonadiabatic, and the power splitting ratio is controlled by the propagation constants of the two single-mode output waveguides. During fabrication, these are controlled by varying the spin cast film thicknesses. For a Y-branch to have equal power outputs, the input mode must couple equally to the supermodes of the branching region. For symmetric structures where the outputs have the same coupling angle, this requires equal effective indices in the two branch arms. For asymmetric Y-branches as shown in Fig. 9, however, a difference in the propagation constants must compensate for the geometric asymmetry present.

To determine the power splitting dependence on the branching angle and propagation constants, we performed 2-D beam propagation simulations. We varied the angle and propagation constants by changing the transition length and waveguide thicknesses, respectively. In the fabrication procedure described in Section III-B1, the input and the upper output waveguides have the same thickness. We therefore made that assumption in our analysis. The index values used corresponded to UV15LV and NOA-73, and the output waveguide separation was a constant 10 μm. The contour plots in Fig. 10 show the splitting ratio, which is defined as the output power ratio of the upper to lower waveguides, as a function of branching angle and upper waveguide thickness. In each plot, the lower waveguide thickness is held to its initial value.

From the contour plots, three design features become apparent. First of all, comparing the three plots shows that a higher tolerance for fabrication errors exists in the thicker waveguide designs. As the waveguide thickness increases, the area for each splitting value ($\pm$10%) becomes larger. Second, 3-dB power splitters possess an optimum branching angle value for fixed waveguide dimensions. For larger angles, the input mode predominantly couples to the lower waveguide because of the geometrical asymmetry and higher radiation loss in the upper branch. For smaller angles, the mode adiabatically selects the output with a higher effective index. Finally, changing the upper waveguide thickness varies the power splitting ratio by affecting the difference in waveguide effective indices. Therefore, fine adjustments of the transition length and waveguide thicknesses allow control of the vertical power

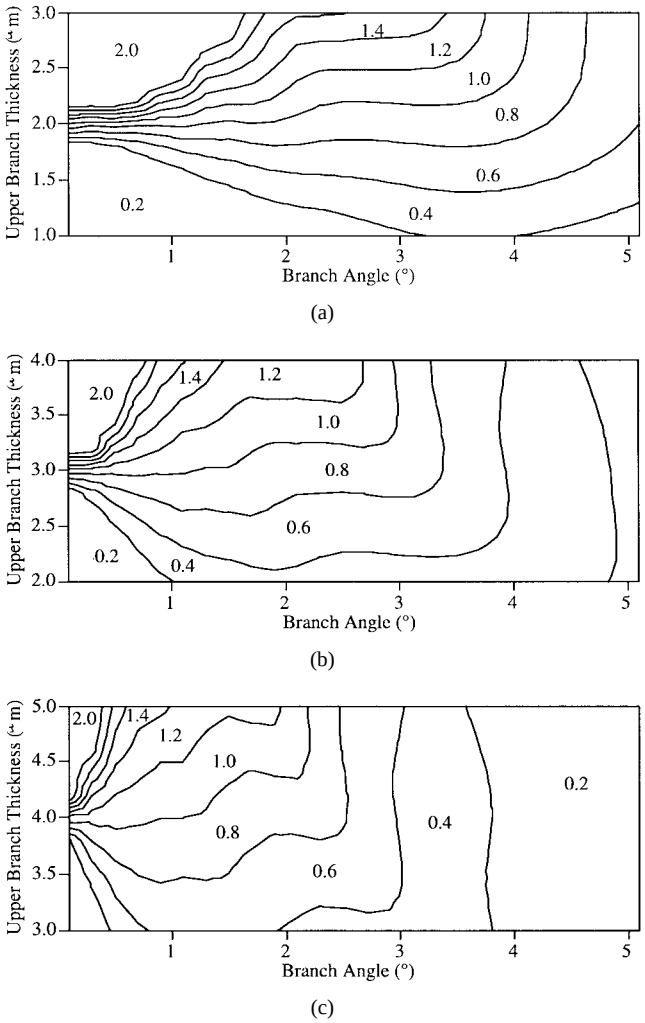

Fig. 10. Y-branch power splitting ratio as a function of upper branch waveguide thickness and ranching angle. Lower branch waveguide thickness held to the constant value indicated for each graph. The contour labels indicate the power splitting ratio values. (a) 2-μm lower waveguide thickness. (b) 3-μm lower waveguide thickness. (c) 4-μm lower waveguide thickness.

splitting ratio through a wide range of values. Waveguide thicknesses close to 3 μm provide the best performance control when considering practical spin cast thicknesses and mode confinement.

Maintaining optical isolation of the output waveguides, another design consideration, requires a minimum thickness of the intermediate cladding layer. For the UV15LV and NOA-73 index values, waveguide thicknesses of 3 μm, output waveguide lengths of 1 cm, and a 6.5-μm vertical waveguide separation yields an isolation between the outputs of $>$30 dB.

Finally, vertical power splitters must minimize radiation loss. The major source of radiation loss is typically the radiation into the waveguide slab modes in the branching region. In this region, the waveguide vertical thickness becomes greater while the ridge height remains constant; this reduces the horizontal confinement and increases the coupling to the slab modes. To prevent this, we designed a dual ridge/channel waveguide structure which maximizes optical confinement throughout the structure. Fig. 11 illustrates the dual ridge/channel structure and also shows core cross sections

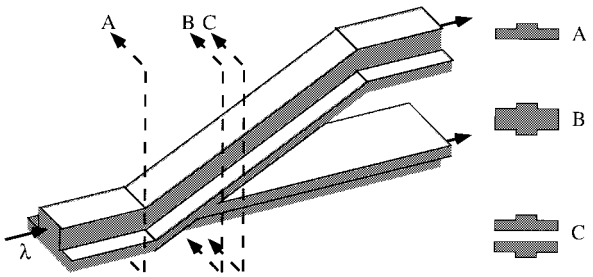

Fig. 11. Vertical power splitter schematic and core cross sections. Cross sections show the transformation of the input ridge waveguide into a dual ridge/channel output structure with high modal confinement. (Only the waveguide core is shown for clarity.)

within the branching region. The presence of both the ridge and the channel of the upper and lower waveguides in the junction allows the core slab region to vertically expand while maintaining the same amount of horizontal confinement. Experimental results shown later support this conclusion.

1) Fabrication: Fabrication of vertical power splitters is illustrated in Fig. 12. The first step involves patterning a Au-coated Si wafer with the horizontal waveguide pattern to provide the necessary marks for aligning the vertically stacked waveguides. This allows horizontal alignment of the waveguides on multiple vertical levels within $\pm$2 μm. Next, a 9.5-μm UV15LV lower cladding was spun, and 0.6-μm-deep, 6-μm-wide channel waveguide patterns were etched. After spin casting NOA-73 for a 3.1-μm lower core thickness [Fig. 12(a)] and a 9.5-μm UV15LV intermediate cladding layer, a 0.5° slope with a depth of 12.6 μm was etched down through the defined lower channel [Fig. 12(b)]. We controlled the etch depth by monitoring the film thickness in a portion of the etched region. Based on monitored lower core and slope dimensions, the upper core thickness necessary for a 3-dB power splitter was determined from the computer analysis. Finally, a 3.2-μm upper core was spin cast and a 0.4-μm upper ridge waveguide pattern etched into the film [Fig. 12(c)]. This transforms the single-ridge waveguide input into a dual single-mode ridge/channel output structure, and it causes the input and upper core waveguides to have the same thickness. All films were UV cured. The final steps include spin casting a 9.5-μm upper cladding layer and cutting the endfaces with a dicing saw to a length of 1.5 cm.

2) Experimental Results: To evaluate the vertical power splitter we used the same experimental setup as that for the vertical bends. Launching light into the single waveguide end showed single-mode performance of the two output waveguides. Likewise, launching light into either of the two branch waveguides excited only a single mode of the base waveguide. Fig. 13 shows the output pattern from each of the structure ends. Adding the output power of the two branch waveguides showed an insertion loss of 4.0 $\pm$ 0.1 dB. Similarly fabricated straight 2-D waveguides resulted in insertion losses of 4.0 $\pm$ 0.2 dB. These insertion losses include input fiber coupling, waveguide propagation, and excess loss due to the vertical slope. Comparing these insertion loss values gives an indication of the excess loss due to the vertical splitting. This low excess loss of $<$0.3 dB existed for both

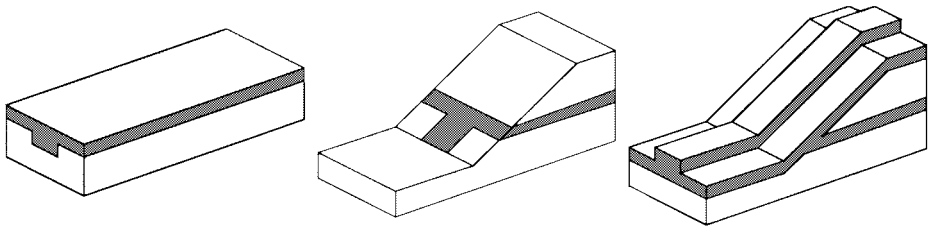

(a) (b) (c)

Fig. 12. Fabrication procedure of vertical power splitters. (a) Channel waveguide defined in lower cladding and core. (b) Middle cladding spin cast and vertical slope etched down through lower core layer. (c) Upper core spin cast and ridge waveguide defined throughout structure.

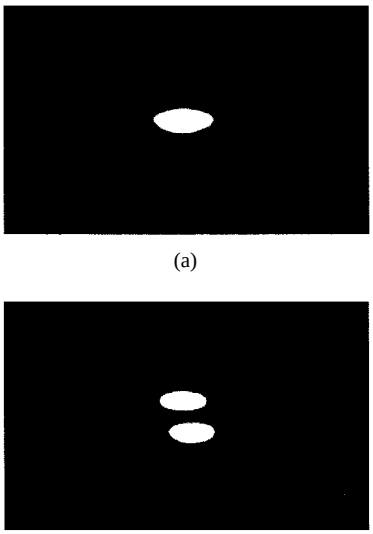

(a) (b)

Fig. 13. Vertical power splitter output patterns for 3-D 1 × 2 structure at $\lambda = 1.31\ \mu$m. (a) Single waveguide end output. Light launched into either branch waveguide. (b) Dual waveguide branched output. Light launched into single base waveguide.

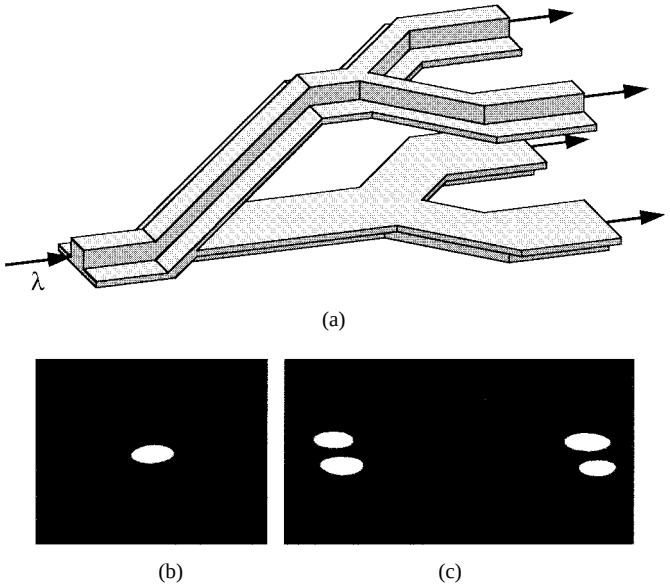

(a) (b) (c)

Fig. 14. Three-dimensional 1 × 4 power splitter waveguide design and output pattern at $\lambda = 1.31\ \mu$m. (a) 1 × 4 power splitter design incorporating one vertical branch and two horizontal Y-branches. (Only the waveguide core is shown for clarity.) (b) Single waveguide end output. Light launched into any of the four branch waveguides. (c) Branched waveguide end output. Light launched into single base waveguide.

polarizations. Additionally, we observed no scattering from above with an infrared camera when launching 40 mW into the waveguides. Furthermore, performance did not degrade for 6-μm-wide waveguides horizontally misaligned by up to 2 μm, as can be seen from the output pattern of Fig. 13(b).

We measured the power splitting ratio (the ratio of the power from the upper waveguide to that from the lower) by focusing the output pattern on a detector 50 cm away and using a knife edge to block the output from either the upper or lower waveguide cores. We measured the output power ratio to be 1.6 ± 0.3. Simulations based on monitored fabrication dimensions predicted a splitting ratio of 1:1. The deviation from the expected output ratio may result from uncertainty in the core thicknesses, uncertainty in the branching angle, and from the different photolithography and etching conditions that each output branch arm may experience. Tighter control of the fabrication conditions should improve the predictability.

Vertically stacking two horizontal Y-branches resulted in a 3-D 1 × 4 splitter. The single-base waveguide first branched vertically and then, immediately, horizontally to produce the four branch waveguides. Fig. 14 shows the device and the output patterns for both the single and branched waveguide ends of the structure. Combining the measured branch output powers showed insertion losses of 4.8 ± 0.1 dB. For comparison, similarly fabricated 2-D 1 × 2 horizontal Y-branches resulted in insertion losses of 4.3 ± 0.6 dB. This increased insertion loss of the 3-D splitter is due to the extra waveguide branching in the vertical direction. The fabricated 1 × 4 splitters had power variations among the 4 output waveguides of 33%. Zero variation corresponds to a 1 × 4 splitter with equal power in all outputs. As measured in the fabricated 2-D 1 × 2 Y-branches, horizontal splitting results in output power variations of 12%. The slightly increased insertion loss and power variation of the 3-D 1 × 4 splitters may result from radiation loss due to the close proximity of the vertical and horizontal waveguide branches, and these may be reduced with longer device lengths.

It is important to consider how fabrication errors affect the predictability of the power splitting ratio. The errors can be in the branch waveguide definition (thickness and ridge/channel height) which varies the effective index of the output guides, and the errors can also occur in the slope definition. From

repeated measurements, we believe the errors in film thickness and ridge/channel height can be held to ± 0.1 μm, and the variation in the index of refraction of the polymers is typically $\pm 10^{-3}$. From a beam propagation analysis, these errors can result in a $\pm 13\%$ variation in the power splitting ratio. The largest source of the variation is due to the relative thickness and ridge/channel height variation of the output waveguides.

In the etching of the slope, both the slope angle and depth of the etch could vary from the expected value. Variations in slope angle occur due to RIE or photolithography repeatabilities when processing $\sim$10-μm feature heights. From our measurements, angles typically fall within $\pm 15\%$ of the target value and etch depth errors are ± 0.1 μm. Based on a beam propagation analysis, these errors can result in a $\pm 7\%$ variation in the power splitting, with the largest variation due to slope angle errors. The vertical depth fabrication error in defining the slope results in a variation of the input base waveguide thickness. The slight effect this thickness has on the power splitting performance allows the vertical power splitters to be built without the need for an etch stop [15].

It may be possible, during the fabrication process, to compensate for accumulated errors in the lower core or slope definition by the appropriate adjustment of the upper core dimensions. These film thickness or slope angle errors can be detected using the profilometer. Also, incorporation of bleachable chromophores should allow *in situ* trimming of device performance in a way similar to 2-D structures [16], [17].

C. Vertical Polarization Splitters

Polarization splitters are used to separate the orthogonal polarization components of the guided waves. These are essential components for coherent receivers and filters employing a polarization diversity design. Three-dimensional integration may find application in these systems to reduce the substrate size required and a vertical polarization splitter would be a key component.

1) Design: The design of vertical polarization splitters [19] follows closely that of the devices described previously, but they rely on the birefringences obtainable in polymers to create a polarization dependent splitting. Fig. 15(a) illustrates this device. Its operation is based on the adiabatic transformation in the junction. The TE mode then propagates to the output with the highest TE effective index, and the TM mode propagates to the output with the highest TM effective index.

Commercially available birefringent and isotropic polymers create the required polarization-dependent difference in effective index. The birefringent polyimides Ultradel 9020D and 7501 (Amoco) composed the lower cladding and core, respectively. The isotropic UV15LV and NOA-73 made up the remaining cladding and core layers, respectively. At $\lambda = 1.31$ μm, 9020D has an index value of 1.522 and 1.495 for TE and TM modes, respectively. 7501 has index values of 1.562 and 1.526 for TE and TM polarizations. Beam propagation simulations determined the optimum waveguide dimensions and branching angle. The fabrication process was similar to that for the vertical power splitter. In [18], the details of the design, fabrication procedure, and a more complete analysis of the vertical polarization splitter are reported.

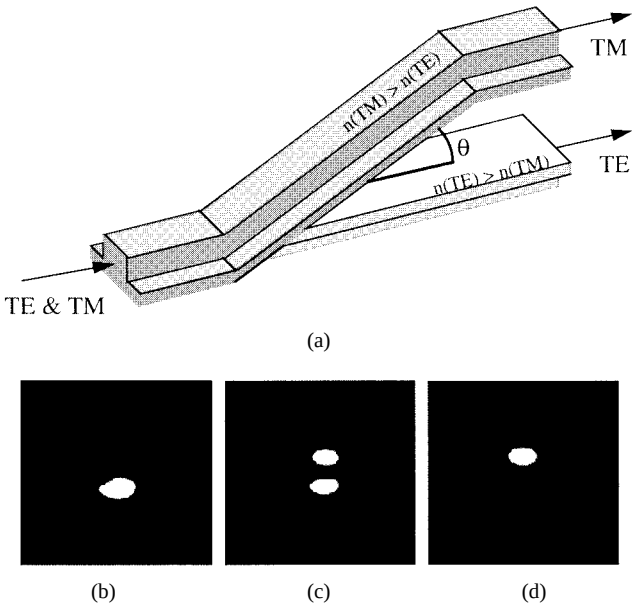

Fig. 15. Vertical polarization splitter design and outputs. All output patterns have light launched into single base waveguide at $\lambda = 1.31$ μm. (a) General waveguide structure. Polarization extinction ratio depends on waveguide birefringence and branching angle. (Only the waveguide core is shown for clarity.) (b) Output pattern with analyzer set for TE polarization. (c) Output pattern with analyzer set for equal TE and TM polarizations. (d) Output pattern with analyzer set for TM polarization.

2) Experimental Results: Light at $\lambda = 1.31$ μm, polarized with equal power in the TE and TM modes, was coupled into the input from a standard optical fiber. The output passed through a polarizer with a 50-dB extinction and collected by a $60\times$ microscope objective lens onto the detector. The TE and TM crosstalk, defined as the ratio of the power in the expected polarization at an output to the power of that polarization in the opposite output, were 17 ± 5 dB and 13 ± 4 dB, respectively.

To demonstrate the single-mode performance of the splitter, we focused the output pattern onto a screen and viewed it with an infrared camera. Fig. 15(b)–(d) shows the output with different analyzer settings. The TE mode output is from the lower waveguide, and the TM is from the upper waveguide. We observed no higher order modes while varying the launch conditions of the input fiber.

D. 3-D Integration of Active and Passive Polymer Devices

One of the advantages of optical polymer technology is the ability to use different types of polymers within the same integrated optical circuit to perform specific functions. For example, electrooptic polymers or light amplifying polymers could be integrated with low loss passive polymers which provide the low loss interconnections. One example of this is the integration of a high speed electro-optic polymer modulator with a Dragone wavelength multiplexer [19] fabricated from passive polymer materials. While the adhesion and patterning problems can sometimes be difficult, the greatest difficulty is often in achieving an optical mode match between the waveguides made from different polymers [20]. The 3-D concept provides a promising method to integrate different polymers while easily solving the mode match problem. In

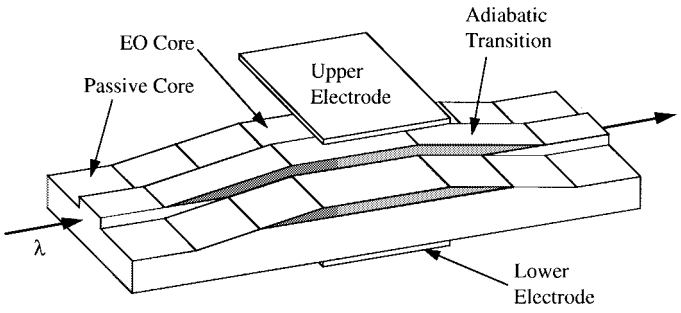

Fig. 16. Polymer electrooptic modulator integrated on top of low-loss passive polymer waveguide. (Cladding layers are not shown for clarity.)

this approach, the interconnect waveguide pattern is first fabricated in a low-loss passive polymer system. The active polymer is then placed on top of this layer and patterned into the area where needed. Vertical coupling structures are then fabricated to channel the light up into the active polymer and then back down again into the passive waveguides. The structures discussed previously provide three-dimensional routing to transfer the beam between the passive and active polymer layers. To demonstrate the feasibility of the approach, we have integrated a poled polymer modulator with passive polymer waveguides.

1) Design: The design of the polymer modulator integrated on top of a passive waveguide is shown in Fig. 16. The upper cladding immediately below the upper electrode and the lower cladding below the lower electrode are not shown for clarity. The passive waveguide was designed to provide a close mode match to the standard 8-μm core fiber and for fiber coupling. The etched vertical taper was designed to adiabatically couple light to the higher index upper core layer which is made of a poled electrooptic polymer. Voltage applied to the electrodes will phase modulate the light or, if configured as a Mach–Zehnder interferometer, will amplitude modulate the light. In the modulator section, the passive core layer serves as the modulator lower cladding. After modulation, the power again transfers to the passive core for further routing. Both the adiabatic slopes and the lower electrode serve as inherent mode filters in the design to minimize stray light that exists in the device. While the mode in the passive waveguide was designed to be symmetric for good fiber coupling, the mode in the modulator was designed to be tightly confined to the active layer for good modulator efficiency. In [21], the design considerations and fabrication procedure are reported in detail.

Fig. 17(a) shows the final device dimensions and scaled cross sections of the passive and active waveguide segments. The passive core and cladding layers consisted of NOA-73 and UV15LV, respectively. Polyurethane containing a tricyano chromophore [22] composed the active upper core. The polyurethane layer was poled by an electric field to obtain the electrooptic effect. The 6.5-cm-long devices were fabricated on 3-in Si wafers as a substrate. The passive core waveguides in both sections were designed to be single mode at 1.31 μm.

2) Experimental Demonstration: An electrooptic phase modulator integrated on top of a passive waveguide was demonstrated at $\lambda = 1.31$ μm. The input light was butt coupled from a fiber into the lower waveguide and contained equal amounts of TE and TM polarization. The near circular mode output profile from the lower waveguide is shown in Fig. 17(b). The polarization of the output was modulated by low-frequency signals applied to the electrodes and the modulation detected by viewing the output through a crossed polarizer. The modulation measured corresponded to an electrooptic coefficient of $r_{33} = 12$ pm/V. Both the contrast observed in the modulation and the insertion loss of the device indicated that essentially all of the transmitted light coupled up into the modulator and back down again. Any light that remained in the lower waveguide is highly attenuated by the lower metal electrode. We also measured the insertion loss of several samples with different lengths of passive and active waveguide regions. Estimating the losses in the passive and active material to be 0.5 and 1.5 dB/cm, respectively, we were again able to confirm that the light couples almost entirely up into the electrooptic polymer and down again. Also, from the known propagation losses in the passive and active materials, we were able to estimate the loss in the transition region to be $\sim$1 dB. From beam propagation studies, we expect the radiation losses in the tapers to be small and, therefore, believe the loss is due to scattering from the surface roughness of the etch. Better fabrication techniques should reduce this loss significantly.

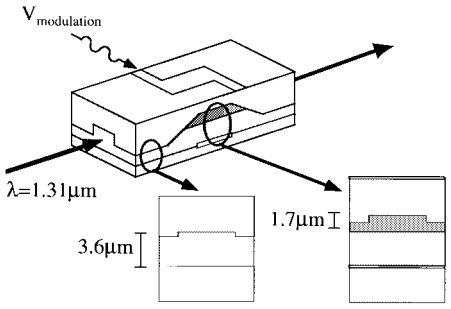

(a)

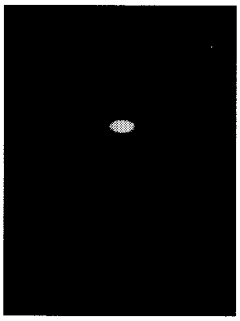

(b)

Fig. 17. Integrated modulator dimensions and optical output. (a) Schematic and scaled cross sections of passive and active waveguide segments. (b) Optical output pattern when light launched into passive waveguide core at $\lambda = 1.31$ μm.

IV. Conclusions

This research shows that 3-D integrated optics in polymer can be a viable approach to significantly increasing the density of integrated optics. There could be numerous applications

for which the substrate area is limited and 3-D circuits are advantageous. The third dimension makes a street–avenue type of interconnection pattern possible without crosstalk when the orthogonal street and avenue waveguides cross. This could make integrated optics competitive with free space optics for a dense optical interconnection network. Perhaps equally important, the 3-D concepts investigated here make it possible to integrate diverse polymer materials, both active and passive, into an optical circuit in a way that solves the difficult impedance and mode-matching problem. While the measured losses in the vertical transition structures are not as low as the very low values predicted in the beam propagation simulations, they are low enough to make us believe that the loss is not caused by any inherent flaw in the concept or design. Instead, they are probably due to fabrication errors and scattering which could be corrected with tighter control and better engineering of the fabrication process.

REFERENCES

[1] L. J. Camp, R. Sharma, and M. R. Feldman, "Guided-wave and free-space optical interconnects for parallel-processing systems a comparison," *Appl. Opt.*, vol. 33, pp. 6168–6180, 1994.

[2] R. A. Norwood, R. Blomquist, L. Eldada, C. Glass, C. Poga, L. W. Shacklette, B. Xu, S. Yin, and J. T. Yardley, "Polymer integrated optical devices for telecommunications applications," in *Polymer Photonic Devices*, B. Kippelen and D. D. C. Bradley, Eds., *Proc. SPIE*, vol. 3281, pp. 2–13, 1998.

[3] L. Palchetti, Q. Li, E. Giorgetti, D. Grando, and S. Sottini, "Photobleaching of polydiacetylene waveguides a characterization of the process and patterning of optical elements," *Appl. Opt.*, vol. 36, pp. 1204–1212, 1997.

[4] M. T. Gale, L. G. Baraldi, and R. E. Kunz, "Replicated microstructures for integrated optics," *Proc. SPIE*, vol. 2213, pp. 2–10, 1994.

[5] A. Chen, F. I. Marti-Carrera, S. Garner, V. Chuyanov, and W. H. Steier, "Fabrication of vertical tapers in polymer thin films by oxygen reactive ion etching with a shadow mask for photonic device applications," in *Organic Thin Films for Photonics Applications, OSA Tech. Dig. Ser.*, 1997, vol. 14, pp. 152–154.

[6] P. R. Ashley and J. S. Cites, "Electro-optic polymer devices for fiber-optic gyros and other applications," in *Organic Thin Films for Photonics Applications, OSA Tech. Dig. Ser.*, 1997, vol. 14, pp. 196–197.

[7] T. J. Suleski and D. C. O'Shea, "Gray-scale masks for diffractive-optics fabrication—I: Commercial slide imagers," *Appl. Opt.*, vol. 34, pp. 7507–7517, 1995.

[8] D. C. O'Shea and W. S. Rockward, "Gray-scale masks for diffractive-optics fabrication—II: Spatially filtered halftone screens," *Appl. Opt.*, vol. 34, pp. 7518–7526, 1995.

[9] E.-B. Kley, F. Thoma, U. D. Zeitner, L. Wittig, and H. Aagedal, "Fabrication of micro optical surface profiles by using gray scale masks," *Proc. SPIE*, vol. 3276, pp. 254–262, 1998.

[10] C. Wachter, Th. Hennig, Th. Bauer, A. Brauer, and W. Karthe, "Integrated optics toward third dimension," in *Integrated Optic Devices II*, G. C. Righini, S. I. Najafi, and B. Jalali, Eds., *Proc. SPIE*, vol. 3278, pp. 102–111, 1998.

[11] C. C. Teng, "Precision measurements of the optical attenuation profile along the propagation path in thin-film waveguides," *Appl. Opt.*, vol. 32, pp. 1051–1054, 1993.

[12] W. J. Minford, S. K. Korotky, and R. C. Alferness, "Low-loss $Ti:LiNbO_3$ waveguide bends at $\lambda = 1.3$ μm," *IEEE J. Quantum Electron.*, vol. QE-18, pp. 1802–1806, 1982.

[13] K. T. Koai and P. L. Liu, "Modeling of $Ti:LiNbO_3$ waveguide devices—Part II: S-shaped channel waveguide bends," *J. Lightwave Technol.*, vol. 7, pp. 1016–1021, 1989.

[14] W. K. Burns and A. F. Milton, "Mode conversion in planar-dielectric separating waveguides," *IEEE J. Quantum Electron.*, vol. QE-11, pp. 32–39, 1975.

[15] S. Kalluri, M. Ziari, A. Chen, V. Chuyanov, W. H. Steier, D. Chen, B. Jalali, H. Fetterman, and L. R. Dalton, "Monolithic integration of waveguide polymer electrooptic modulators on VLSI circuitry," *IEEE Photon. Technol. Lett.*, vol. 8, pp. 644–646, 1996.

[16] A. Chen, V. Chuyanov, F. I. Marti-Carrera, S. Garner, W. H. Steier, S. S. H. Mao, Y. Ra, and L. R. Dalton, "Fast trimming of electro-optic polymer waveguide Y-branches by post-photobleaching for tuning the power splitting ratio," *Proc. SPIE*, vol. 3147, pp. 268–274, 1997.

[17] A. Chen, V. Chuyanov, F. I. Marti-Carrera, S. Garner, W. H. Steier, S. S. H. Mao, Y. Ra, L. R. Dalton, and Y. Shi, "Trimming of polymer waveguide Y-junction by rapid photobleaching for tuning the power splitting ratio," *IEEE Photon. Technol. Lett.*, vol. 9, pp. 1499–1501, 1997.

[18] S. M. Garner, V. Chuyanov, S.-S. Lee, A. Chen, W. H. Steier, and L. R. Dalton, "Vertically integrated waveguide polarization splitters using polymers," *IEEE Photon. Technol. Lett.*, vol. 11, pp. 842–844, 1999.

[19] C. Dragone, "An $N \times N$ optical multiplexer using a planar arrangement of two star couplers," *IEEE Photon. Technol. Lett.*, vol. 3, pp. 812–815, 1991.

[20] T. Watanabe, M. Hikita, M. Amano, Y. Shuto, and S. Tomaru, "Vertically stacked coupler and serially grafted waveguide hybrid waveguide structures formed using an electro-optic polymer," *J. Appl. Phys.*, vol. 83, pp. 639–649, 1998.

[21] S. M. Garner, V. Chuyanov, A. Chen, W. H. Steier, and L. R. Dalton, "Three-dimensional integration of polymer electro-optic modulators," in *IEEE/LEOS Organic Optics and Optoelectronics Topical Meeting*, Monterey, CA, July 1998, paper FC3.

[22] F. Wang, A. S. Ren, M. He, A. W. Harper, L. R. Dalton, S. M. Garner, H. Zhang, A. Chen, and W. H. Steier, "High electro-optic coefficient from a polymer containing high $\mu\beta$ chromophores," *Polymer Material Science and Engineering*, vol. 78, pp. 42–43, 1998.

Sean M. Garner, photograph and biography not available at the time of publication.

Sang-Shin Lee, photograph and biography not available at the time of publication.

Vadim Chuyanov, photograph and biography not available at the time of publication.

Antao Chen, photograph and biography not available at the time of publication.

Araz Yacoubian, photograph and biography not available at the time of publication.

William H. Steier, photograph and biography not available at the time of publication.

Larry R. Dalton, photograph and biography not available at the time of publication.